



Contents lists available at ScienceDirect

Nuclear Instruments and Methods in Physics Research A

journal homepage: www.elsevier.com/locate/nima

A compressed sensing based reconstruction algorithm for synchrotron source propagation-based X-ray phase contrast computed tomography

Ali Melli^{a,*}, Khan A. Wahid^a, Paul Babyn^b, James Montgomery^c, Elisabeth Snead^d, Ali El-Gayed^c, Murray Pettitt^e, Bailey Wolkowski^e, Michal Wesolowski^b

^a Department of Electrical and Computer Engineering, University of Saskatchewan, Saskatoon, SK, Canada

^b Department of Medical Imaging, University of Saskatchewan, Saskatoon, SK, Canada

^c College of Medicine, University of Saskatchewan, Saskatoon, SK, Canada

^d Western College of Veterinary Medicine, University of Saskatchewan, Saskatoon, SK, Canada

^e College of Agriculture and Bioresources, University of Saskatchewan, Saskatoon, SK, Canada

ARTICLE INFO

Article history:

Received 14 April 2015

Received in revised form

23 July 2015

Accepted 5 October 2015

Keywords:

Synchrotron source imaging
Propagation-based X-ray phase contrast
computed tomography
Compressed sensing
Low X-ray dose computed tomography
reconstruction algorithm

ABSTRACT

Synchrotron source propagation-based X-ray phase contrast computed tomography is increasingly used in pre-clinical imaging. However, it typically requires a large number of projections, and subsequently a large radiation dose, to produce high quality images. To improve the applicability of this imaging technique, reconstruction algorithms that can reduce the radiation dose and acquisition time without degrading image quality are needed. The proposed research focused on using a novel combination of Douglas–Rachford splitting and randomized Kaczmarz algorithms to solve large-scale total variation based optimization in a compressed sensing framework to reconstruct 2D images from a reduced number of projections. Visual assessment and quantitative performance evaluations of a synthetic abdomen phantom and real reconstructed image of an ex-vivo slice of canine prostate tissue demonstrate that the proposed algorithm is competitive in reconstruction process compared with other well-known algorithms. An additional potential benefit of reducing the number of projections would be reduction of time for motion artifact to occur if the sample moves during image acquisition. Use of this reconstruction algorithm to reduce the required number of projections in synchrotron source propagation-based X-ray phase contrast computed tomography is an effective form of dose reduction that may pave the way for imaging of in-vivo samples.

© 2015 Elsevier B.V. All rights reserved.

1. Introduction

One limitation of conventional X-ray computed tomography (CT) is that the tissue attenuation of soft tissue structures are similar in hard X-rays and these tissues cannot be examined without using iodine. For example, conventional X-ray CT cannot discriminate minor differences in tissue density/variation which occurs in the early stages of prostate cancer [1]. To address this issue, X-ray phase contrast computed tomography (XPC-CT) [2,3] has been utilizing the change in phase of X-ray beams as they pass through a sample rather than solely relying on the amplitude attenuation, as is the case with conventional X-ray CT. The phase sensitivity to mild density variation in the soft tissues is three orders of magnitude higher than the amplitude sensitivity at

10–100 keV range [4]. Therefore, XPC-CT has an improved ability to differentiate amongst different soft tissue structures without need for exogenous contrast.

There are several experimental setups available to generate X-ray phase contrast images. Among them, propagation-based XPC-CT (also known as “in-line holography”) has a simple setup with high spatial resolution (a few tens of microns) and low dose capability. Some encouraging results have been reported for the application of this technique in clinical experiments [5]. Phase-contrast images can be generated with this technique when the X-ray source provides a spatially coherent illumination [6]. Propagation-based XPC-CT techniques have been developed with synchrotrons sources as they provide spatially coherent high brilliance radiation [7,8]. The experimental setup of this synchrotron based technique is like the setup used in radiography i.e. synchrotron X-ray source, the sample and the detector are inline, without any optical element between the sample and the detector. Instead of placing the detector directly behind the sample, which is convenient in radiography, it is placed in some distance from the

* Correspondence to: Department of Electrical and Computer Engineering, University of Saskatchewan, Room 2C64, 57 Campus Drive, Saskatoon, SK, Canada S7N5A9. Tel.: +1 306 203 3988; fax: +1 306 966 5407.

E-mail address: sem649@mail.usask.ca (A. Melli).

sample (often called propagation distance). As a result, the X-rays that are refracted by different tissues due to different refractive indices inside the sample can interfere with unaffected beam on the detector [9]. The phase contrast image formed in the detector is sensitive to abrupt variations of refractive indices; so the structural boundaries between different tissues inside the sample are enhanced in this technique [10].

With this capability, the synchrotron-based propagation-based XPC-CT can provide higher tissue contrast and spatial resolution of prostate images compared with conventional X-ray CT [11]. To achieve the requisite spatial resolution, a large number of projection views (> 1000) is necessary to discriminate fine details of small structures in the sample field of view [12–14]. This exposes the specimen to high radiation that would be detrimental when imaging a live patient or animal in-vivo. One approach to decrease total X-ray dose and imaging time is to reduce exposure time per projection which is the only parameter that can be used to control the amount of X-ray dose in each projection since the photon brightness of synchrotron X-ray is fixed [15]. However, the minimum exposure time is limited by detector sensitivity and readout speed. Also, low exposure time generally results in lower projection signal to noise and accordingly lower quality of reconstructed image [16]. Sparse-view imaging technique is another approach which can reduce the number of projections and consequently the total X-ray dose and imaging time, while maintaining acceptable diagnostic image quality.

Analytical algorithms such as Filtered Back Projection (FBP) remains the standard reconstruction algorithm for most commercial CT scanners. When sparse-view imaging technique is used with this algorithm, serious aliasing artifacts, such as sharp streaks, can be observed in the reconstructed images [17]. Unlike analytical algorithms, iterative algorithms are increasingly used for reconstruction of images when noisy and incomplete projection data are available [18]. Iterative algorithms are based on solving a system of linear equations subject to the constraints that are obtained from prior information about the reconstructed image. A number of well-known iterative algorithms include: Projection onto Convex Sets (POCS) [19], Maximum Likelihood Expectation Maximization (MLEM) [20] and Adaptive Steepest Descent – Projection onto Convex Sets (ASD-POCS) [21]. POCS, also known as the alternating projection algorithm, has relatively low computational complexity and is utilized to find the intersection point of two or more closed convex sets to solve a system of linear equations. The MLEM algorithm attempts to solve a system of linear equations which have non-negative coefficients in both the system matrix and observation vector. The ASD-POCS algorithm attempts to reconstruct the assumed non-negative images by minimizing the total variation seminorm in the image, subject to the constraint that the estimated projected data should be within a known tolerance of the acquired data.

Recently, compressed sensing (CS) theory has attracted huge attention in the imaging community because of its ability to formulate the principles for exact recovery of signal from highly incomplete frequency information [22,23]. This theory is applicable to images that are compressible in a predefined basis/frame such as wavelet, gradient, Fourier i.e. most of the transformed image pixels should be approximately zero. Use of the gradient basis such as total variation (TV) has proven advantageous for tomographic images as they have uniform tissues with only abrupt changes at boundaries [24]. It motivates us to propose a CS-based algorithm to reconstruct large-scale high resolution images from significantly reduced projection data.

The algorithm proposed in this paper aims to recover the image from sparse-view synchrotron source propagation-based phase contrast data using a combination of Douglas–Rachford splitting (DRS) and randomized Kaczmarz algorithms to optimize large-scale TV-based optimization in a compressed sensing framework.

The DRS algorithm was first formulated in [25] and is applicable to convex programming in which a large problem can be divided into smaller and easier to solve problems. The randomized Kaczmarz algorithm is an iterative algorithm that can be used to solve linear equations. One application of this algorithm in solving linear equations is illustrated by reconstruction of a band-limited function from non-uniform spaced sampling values in [26]. We hypothesize that the proposed algorithm is able to reconstruct smooth image regions while preserving prominent edges at the borders of different regions better than existing reconstruction algorithms.

Our proposed algorithm may also be applicable to other synchrotron-based medical imaging technologies including micro computed tomography (micro-CT) [27], K-edge subtraction computed tomography (KES-CT) [28] and computed tomography of diffraction enhanced imaging (DEI-CT) [29] to reduce radiation dose and imaging time.

2. Material and methods

2.1. XPC-CT data acquisition

Phase contrast projection data were collected at the Biomedical Imaging and Therapy Bending Magnet (BMIT-BM) Beamline at the Canadian Light Source, Inc. (CLS) [15]. This is a bend magnet beamline with a field strength of 1.354 T. The ring energy is 2.9 GeV and the storage ring current is a maximum of 250 mA operating in decay mode. The critical energy of the bend magnet source is 7.57 keV. The Beamline uses a Si (2,2,0) Bragg double crystal monochromator at a distance of 13.2 m from the source. A formalin fixed canine prostate was suspended in a plastic specimen tube within Knox Gelatin.¹ The sample was placed on a rotating mechanical stage that was 25 m away from the synchrotron source so that the X-ray beam can be assumed to be parallel. The X-ray beam energy was 30 keV. A Photonic Science VHR-90 radiation detector² (FOP coupled CCD detector, 18.67 μm × 18.67 μm pixel size) was placed 5 m behind the sample to allow propagation phase contrast imaging. The sample was then rotated over 180.096° and 3751 projections were taken, each at a rotational step size of 0.048°. Dark and flat calibration images were taken before and after the tomogram projections for each 3.1 mm thick slice of the prostate gland under scan. The detector processed these projections in a 12 bit TIFF greyscale digital format.

Synchrotron source propagation-based XPC-CT raw data requires preprocessing prior to reconstruction, including dark and flat field calibration, rotation center alignment and ring artifact correction. These modifications should be done before application of the reconstruction algorithm [30]. NRecon developed in Bruker microCT³ [31] and PITRE (Phase-sensitive X-ray Image processing and Tomography REconstruction) [32] are two commercial software systems used at the Canadian Light Source to preprocess raw data and reconstruct tomographic images. PITRE offers parallel-beam tomographic reconstruction for phase contrast CT data. In this program, dark and flat field calibration is performed on the projections. After sinogram generation, PITRE implements image cutting, extended field of view CT data conversion, ring artifacts correction and rotation center alignment. On the other hand, NRecon is a general-purpose and easy to use software. It does not support some preprocessing tasks which are required for preparation of synchrotron CT raw data for reconstruction; for

¹ Knox Gelatin, Associated Brands LP, Toronto, ON.

² Photonic Science VHR90, Photonic Science, Ltd., Millham, Mountfield, UK.

³ Bruker microCT, Kontich, Belgium.

example, the software does not implement dark and flat field calibration. Consequently, a macro plugin for ImageJ [33] is used for dark and flat field calibration. After opening calibrated raw data in NRecon, it will automatically find the best settings for rotation center alignment, ring artifact correction and smoothing filter. NRecon needs a large number of angular projections to generate the reference image and the corresponding sinogram dataset for performance evaluation of different algorithms.

2.2. Sparse view imaging

It is possible to reconstruct a significant (high signal to noise) 3D object from non-significant (low signal to noise) 2D projections, if the number of projections is large [34]. In practice, the upper limit to the number of projections over which the dose can be fractionated is given by the requirement that the 2D projections have to be aligned to a common origin before a 3D reconstruction can be computed [35]. After trial and error, we have concluded that shortening the exposure time per projection to less than 100 milliseconds would lead to significant decrease in projection signal to noise so the requirement that the 2D projections have to be aligned to a common origin may be violated. Each prostate requires between 6 and 12 slices to image the whole gland with each slice consisting of nearly 4000 projections as per Nyquist-Shannon sampling theory to guarantee appropriate reconstruction [14,36]. As a result, high total radiation exposure is inevitable which is harmful to live bodies. Besides, an average acquisition time of 60 min to image the whole gland tends to be too long for live bodies because motion artifact may occur if the sample moves during image acquisition. The compressed sensing theory intends to reconstruct images with a good accuracy from considerably fewer projections than required by the Nyquist-Shannon theory [37]. The proposed compressed sensing based method reduces the number of projections to proportionally decrease radiation dose as well as acquisition time while maintaining acceptable diagnostic contrast and spatial resolution in the reconstructed image.

2.3. Imaging model and optimization formulation

In the XPC-CT experiment, the collected noisy data $b = (b_1, b_2, \dots, b_M)^T$ and the reconstructed image $x = (x_1, x_2, \dots, x_N)^T$, where T is the transpose of a vector, can be inferred as a discrete linear system:

$$b = Ax + n \quad (1)$$

where A represents an underdetermined $M \times N$ ($M < N$) system matrix that models a parallel X-ray beam forward projection and n represents zero mean additive white Gaussian noise model. The objective is to accurately reconstruct an image from incomplete noisy data. When $M < N$, a unique solution of Eq. (1) does not exist leading to an infinite number of solutions. To solve this problem, regularization should be applied which outlines a weak smoothness constraint for selecting a solution from a set of infinite solutions. In other words, the regularization controls the trade-off between fidelity to measured data and to prior information (smoothness of computed tomography images), so the regularized energy function to be minimized is a weighted sum of two functions as shown below in Eq. (2):

$$J(x, \alpha) = \frac{1}{2} \|Ax - b\|_2^2 + \alpha J(x) \text{ with } \alpha > 0 \quad (2)$$

where the first term is the data fidelity function and the second term is the regularizing function. One well known regularizing function is Tikhonov function [38] where the $J(x)$ is the squared L2-norm (the square root of the sum of the squared pixel values, i.e. $\|x\|_2^2 = x_1^2 + x_2^2 + \dots + x_n^2$) of an image. However, Tikhonov

function has a tendency to make images excessively smooth and poorly preserves important image characteristics, such as sharp edges. As a result, L1-norm (the sum of the absolute pixel values, i.e. $\|x\|_1 = |x_1| + |x_2| + \dots + |x_n|$) of the gradient image also known as total variation (TV) function [39] is commonly used as the regularizing function for image reconstruction [40]. The benefit of TV regularization over Tikhonov quadratic regularization is that it makes the recovered image sharper by accurately preserving the edges especially in piecewise smooth images and also the solution is insensitive to some data values that are far away from others [41].

According to the above description, let us consider a TV-based optimization problem called *generalized Lasso* [42]:

$$\underset{x}{\text{Minimize}} \frac{1}{2} \|Ax - b\|_2^2 + \lambda \|Fx\|_1 \quad (3)$$

Here, parameter λ compromises between data fidelity and regularizing function. Let x_{ij} denote the pixel in the i^{th} row and j^{th} column of an $n \times n$ image x and define the difference operators as follows:

$$Fh_{ij}x = \begin{cases} x_{i+1,j} - x_{i,j} & i < n \\ 0 & i = n \end{cases} \quad Fv_{ij}x = \begin{cases} x_{i,j+1} - x_{i,j} & j < n \\ 0 & j = n \end{cases}$$

$$F_{ij}x = \begin{pmatrix} Fh_{ij}x \\ Fv_{ij}x \end{pmatrix} \quad (4)$$

where $Fh_{ij}x$ and $Fv_{ij}x$ are horizontal and vertical difference operators respectively. With this definition, the second term in Eq. (3) is called TV operator. The difficulties that arise in solving this optimization problem are related to non-differentiability of L1-norm $\|Fx\|_1$ at zero which leads to numerical instabilities for common gradient-based optimization algorithms. Some are related to noisy data and ill-conditioning of the system matrix which causes the solution of optimization problem deviate strongly from noise-free solution. Lastly, optimization in large-scale makes some methods which use second order primal-dual interior-point inefficient and impractical.

2.4. Proposed algorithm

Our approach to solve the problem is to modify Eq. (3) into an equivalent constrained optimization problem as shown in Eq. (5) below:

$$\underset{x}{\text{Minimize}} \frac{1}{2} \|Ax - b\|_2^2 + \lambda \|z\|_1 \text{ subject to } Fx - z = 0 \quad (5)$$

In order to find a global minima of a function subject to equality constraint, an unconstrained optimization problem should be formed as follows:

$$\underset{x}{\text{Minimize}} L_\rho(x, z, y) = \frac{1}{2} \|Ax - b\|_2^2 + \lambda \|z\|_1 + y^T(Fx - z) + \frac{\rho}{2} \|Fx - z\|_2^2 \quad (6)$$

where y^T is called the vector of dual variables and $\rho > 0$ is called the penalty parameter [43]. The benefit of including the penalty term $\frac{\rho}{2} \|Fx - z\|_2^2$ is to ensure global convergence which means better handling of ill-conditioned measurement. The measurement equation $b = Ax$ is ill-conditioned because small changes in b or even A may lead to large changes in solution vector x . Defining the residual $r = Fx - z$ and using Eq. (7) that is a simple mathematic formula, Eq. (6) can be rewritten in a new form that is illustrated in Eq. (8) by merging the linear function $y^T(Fx - z)$ and quadratic function $\frac{\rho}{2} \|Fx - z\|_2^2$, and scaling the dual variables.

$$y^T r + \frac{\rho}{2} \|r\|_2^2 = \frac{\rho}{2} (\|r + u\|_2^2 - \|u\|_2^2) \quad u = \frac{y}{\rho} \quad (7)$$

$$\begin{aligned} 1 & \text{Minimize}_x L_\rho(x, z, y) = \frac{1}{2} \|Ax - b\|_2^2 + \lambda \|z\|_1 + \frac{\rho}{2} \|Fx - z + u\|_2^2 - \frac{\rho}{2} \|u\|_2^2 \\ 2 & \end{aligned} \quad (8)$$

3 We propose to solve the minimization problem in Eq. (8) by
4 applying Douglas–Rachford Splitting (DRS) algorithm [44]. Using
5 this algorithm, Eq. (8) will be decomposed into sub optimization
6 problems by separately minimizing it with respect to x and z while
7 assuming the other variable to be fixed. This method is most useful
8 when the optimization problem with respect to x and z
9 (i.e. Eqs. (9) and (10)) can be efficiently evaluated whereas the
10 joint minimization of Eq. (8) is not easy to evaluate. This mini-
11 mizing process is completed by a dual variable update operation.
12 The sub optimization steps are given below:

13 Loop

$$14 \quad x^{k+1} = \text{Minimize}_x \frac{1}{2} \|Ax - b\|_2^2 + \frac{\rho}{2} \|Fx - z^k + u^k\|_2^2 \quad (9)$$

$$15 \quad z^{k+1} = \text{Minimize}_z \lambda \|z\|_1 + \frac{\rho}{2} \|Fx^{k+1} - z + u^k\|_2^2 \quad (10)$$

$$16 \quad u^{k+1} = u^k + Fx^{k+1} - z^{k+1} \quad (11)$$

17 Until stop condition is satisfied

18 where k is a loop counter. In each of the x and z -update steps,
19 $L_\rho(x, z, y)$ is minimized over the corresponding variable, using the
20 most recent value of the other variables x , z and u . The fixed terms
21 such as $\frac{\rho}{2} \|u\|_2^2$ that are ineffective in finding the optimal solution
22 are removed from sub optimization update steps. Structures in
23 Eq. (9) and Eq. (10) can be utilized to find closed form solution or
24 an iterative formulation to update x and z efficiently.

25 Although $\lambda \|z\|_1$ in Eq. (10) is not differentiable, sub differential
26 calculus techniques [45] can be used to compute a closed form
27 formula. The solution is an element-wise soft threshold formula as
28 given below:

$$29 \quad z^{k+1} = S_{\frac{\lambda}{\rho}}(Fx^{k+1} + u^k) \quad (12)$$

30 where operator S is defined as follows:

$$31 \quad S_k(a) = \begin{cases} a - \kappa & a > \kappa \\ 0 & |a| \leq k \\ a + \kappa & a < -k \end{cases} \quad (13)$$

32 This formula shrinks the vector elements toward zero without
33 making any discontinuity. The next step is to find a closed form
34 formula to solve optimization problem in Eq. (9). This is a least
35 square minimization problem and the solution is as follows [46]:

$$36 \quad x^{k+1} = (A^T A + \rho F^T F)^{-1} (A^T b + \rho F^T (z^k - u^k)) \quad (14)$$

37 According to Eq. (14), a system of linear equations with the
38 coefficient matrix $A^T A + \rho F^T F$ and right hand matrix $A^T b + \rho F^T (z^k - u^k)$
39 should be solved to update x .

40 Here, we propose to use the randomized Kaczmarz iterative
41 algorithm for solving large-scale linear systems. The algorithm
42 converges to the accurate answer without a need to inverse the
43 coefficient matrix. The randomized Kaczmarz algorithm is as fol-
44 lows [26]:

45 **Algorithm (Randomized Kaczmarz algorithm):** Assume $Ax = b$,
46 $A \in R^{M \times N}$ to be a system of linear equations and x_0 be the first
47 approximation of the final solution. We represent the rows of A by

48 a_1, a_2, \dots, a_M and let $b = (b_1, b_2, \dots, b_M)^T$. The iterative formula to
49 compute the final solution is as follows:

$$50 \quad x^{k+1} = x^k + \frac{b_{r(i)} - \langle a_{r(i)}, x_k \rangle}{\|a_{r(i)}\|_2^2} \quad (15)$$

51 where $r(i)$ is randomly selected with probability proportional to
52 $\|a_{r(i)}\|_2^2$ from the number set $\{1, 2 \dots M\}$.

53 The proposed algorithm is summarized below:

54 Initialize: A , b , F and $\rho, \lambda > 0$

55 Loop

56 Compute x^{k+1} using Eq. (14) with $z = z^k$, $u = u^k$ - randomized
57 Kaczmarz

58 Compute z^{k+1} using Eq. (12) with $x = x^{k+1}$, $u = u^k$ - soft threshold

59 Compute u^{k+1} using Eq. (11) with $z = z^{k+1}$, $x = x^{k+1}$ and $k = k + 1$

60 Until $\frac{\|x^{k+1} - x^k\|_2}{\max\{\|x^k\|_2, 1\}} < \epsilon$ (tolerance ϵ , e.g. 10^{-4})

61 We can now “warm start” each iteration in randomized Kacz-
62 marz algorithm by initializing each iteration with solution x_k
63 which is obtained in the previous DRS iteration. See [47] for fur-
64 ther explanation. Therefore, the number of x -update iterations in
65 randomized Kaczmarz algorithm (inner iterations) reduces to a
66 small number while the global DRS algorithm (outer iterations)
67 converges. This can provide considerable time savings.

68 The proposed algorithm was implemented using MATLAB
69 R2014b. Element-wise soft threshold formula in Eq. (12) was
70 implemented by “wthresh” command in the MATLAB environ-
71 ment. Randomized Kaczmarz algorithm in Eq. (14) was imple-
72 mented by “randkaczmarz” command which is included in the
73 “AIR Tools” package in MATLAB [48].

2.5. Assessment of image quality

74 Both visual and quantitative evaluations are used to compare
75 the performance of the proposed algorithm with other related
76 algorithms. They are described in the next section.

2.5.1. Quantitative based assessment

77 Three quantitative metrics, structural similarity (SSIM) index,
78 Peak Signal to Noise Ratio (PSNR), and Relative Error (RE) are used
79 to evaluate the quality of reconstructed images. The SSIM is a
80 degradation-based quality metric for measuring the structural
81 similarity between two images and it has been proven to be
82 consistent with human visual system [49]. If ρ and t are two local
83 image windows selected from the same position of two input
84 images, SSIM can be calculated as:

$$85 \quad \text{SSIM}(\rho, t) = \frac{2\mu_\rho\mu_t + C1}{\mu_\rho^2 + \mu_t^2 + C1} \cdot \frac{2\sigma_\rho\sigma_t + C2}{\sigma_\rho^2 + \sigma_t^2 + C2} \cdot \frac{\sigma_{\rho t} + C3}{\sigma_\rho\sigma_t + C3} \quad (16)$$

86 where μ_ρ and μ_t are the averages, σ_ρ and σ_t are the standard
87 deviations and $\sigma_{\rho t}$ is the covariance of the local windows.
88 $2C3 = C2$, $C1$ are constants to stabilize division. The overall SSIM
89 index is calculated by averaging the SSIM map along the entire
90 image. A higher SSIM index indicates superior image quality.

91 The PSNR is an error sensitive quality metric used to estimate
92 reconstruction accuracy and is defined as follows:

$$93 \quad \text{PSNR(db)} = 10 \log_{10} \left(\frac{\text{Peak}^2}{\text{MSE}} \right) \quad (17)$$

94 where Peak is the highest pixel value, e.g. in the case of 12 bit
95 pixel representation, it is 1023; MSE is the mean square error
96 between the reconstructed and reference images.

97 Lastly, Relative Error between a reconstructed and reference
98 image is defined as follows:

$$99 \quad \text{RE}(\%) = \frac{\|x_{\text{ref}} - x_{\text{rec}}\|_2}{\|x_{\text{ref}}\|_2} \times 100 \quad (18)$$

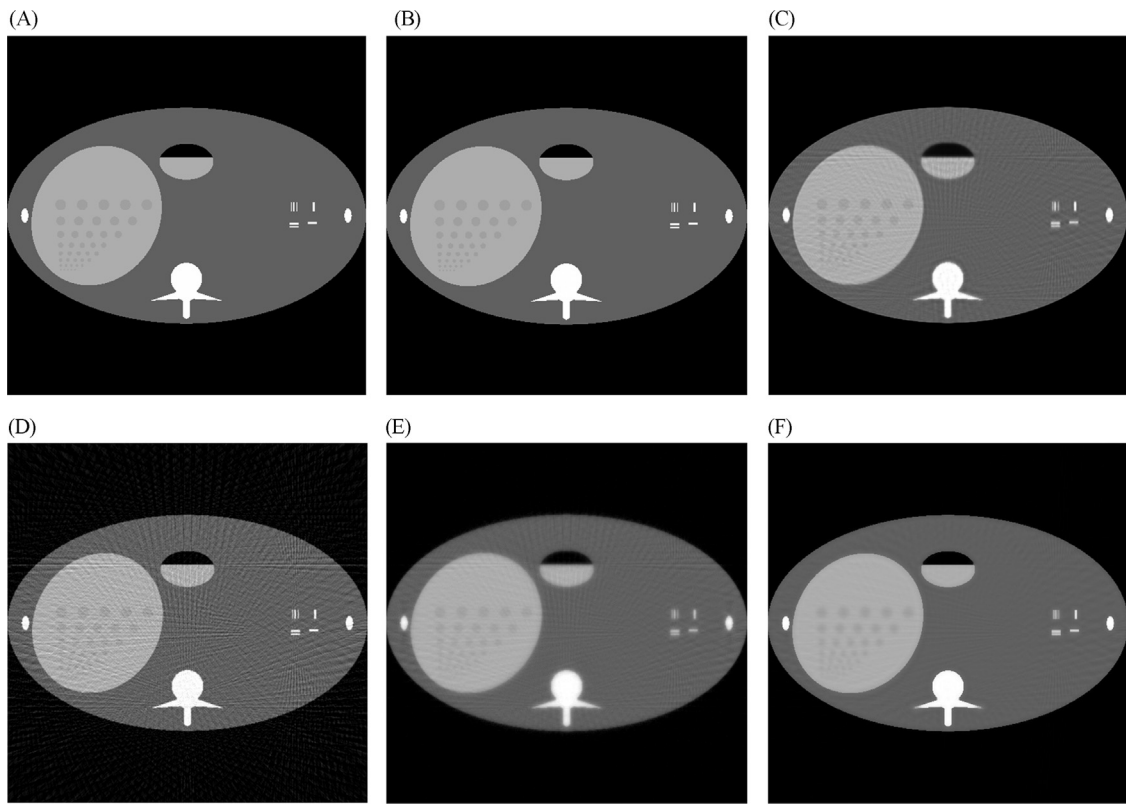


Fig. 1. Reconstructed synthetic abdomen phantom images with 20% of projected data (A) Reference, (B) Proposed, (C) MLEM, (D) FBP, (E) POCS and (F) ASD-POCS.

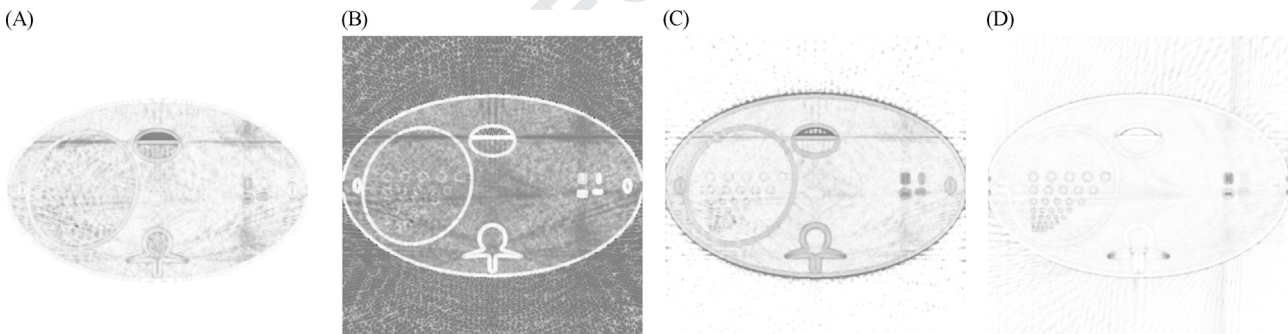


Fig. 2. SSIM index map of images reconstructed with 20% of projected data (A) MLEM, (B) FBP, (C) POCS, (D) ASD-POCS.

2.5.2. Visual assessment

The images were reconstructed by five different algorithms at four different sampling rates of projected data. In addition to comparison of these reconstructed images, enlarged regions of interest from these images were also compared with the corresponding region of interest from reference image to visually assess the reconstruction process.

3. Experimental results and discussion

The proposed algorithm along with four existing methods were used to reconstruct a synthetic abdomen phantom image and a 3.1 mm thick single transverse slice of a canine prostate. In both cases, the reconstruction algorithms were implemented at different number of projected data that are uniformly extracted from a full dataset. MATLAB R2014b software was used to implement the

algorithms on a Desktop PC with Intel® Xeon® CPU 2 GHz processor and 32 GB memory.

3.1. Reconstructed images of synthetic abdomen phantom

A noise-free synthetic abdomen phantom [50] is used as the first experiment because it covers large and small structures. The size of this phantom image is 512×512 pixels. Five images were reconstructed using FBP, POCS, MLEM, ASD-POCS and the proposed algorithm where equally spaced 7%, 10%, 20% and 40% of the full dataset have been used. Fig. 1 shows the reference image compared with reconstructed images using 20% (72 views) of the full dataset. As it is evident from Fig. 1, the proposed algorithm is able to perfectly reconstruct the phantom image using only 20% of projected data. Fig. 2 shows structure similarity index maps for four algorithms so that a pixel-by-pixel comparison can be performed. The SSIM map was not shown for the proposed algorithm

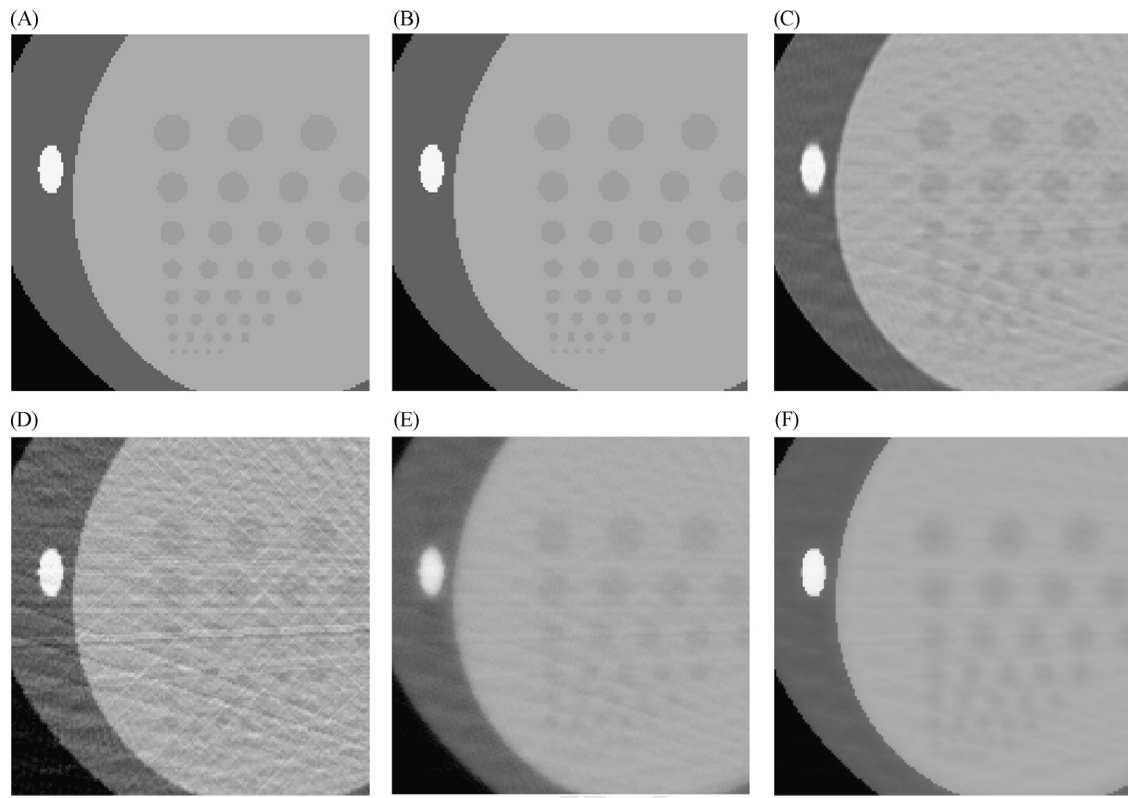


Fig. 3. Enlarged region of interest in Fig. 1 (A) Reference, (B) Proposed, (C) MLEM, (D) FBP, (E) POCS, (F) ASD-POCS.

Table 1
Quality metrics of reconstructed synthetic abdomen phantom.

Data percentage	7% Method	SSIM	RE%	PSNR	10% SSIM	RE%	PSNR	20% SSIM	RE%	PSNR	40% SSIM	RE%	PSNR
Proposed	0.97	0.93	50.64	1	0.05	74.78	1	0.02	82.60	1	0.01	84.83	
FBP	0.12	34.96	19.18	0.14	29.19	20.75	0.27	16.57	25.67	0.55	9.6	30.41	
POCS	0.82	13.28	27.59	0.84	11.59	28.77	0.89	9.82	30.21	0.93	9.21	30.77	
MLEM	0.88	11.44	28.89	0.89	9.39	30.60	0.91	6.98	33.17	0.96	5.54	35.17	
ASD-POCS	0.88	10.8	29.39	0.93	7.32	32.76	0.96	4.6	36.80	0.98	2.6	41.75	

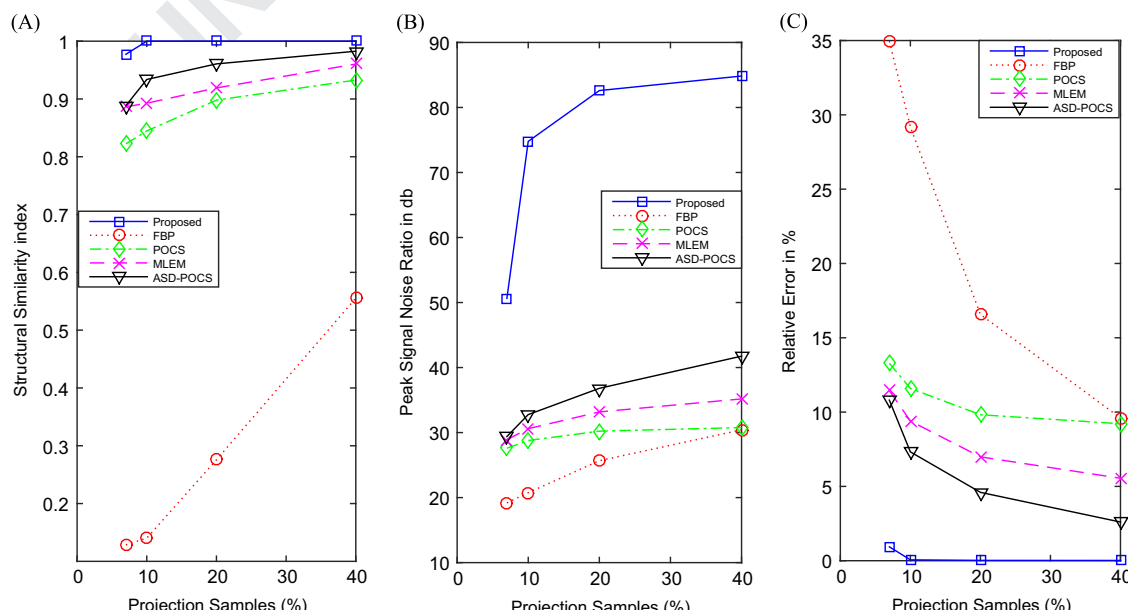


Fig. 4. Phantom quality metrics vs percentage of projected data (A) SSIM, (B) PSNR, (C) RE.

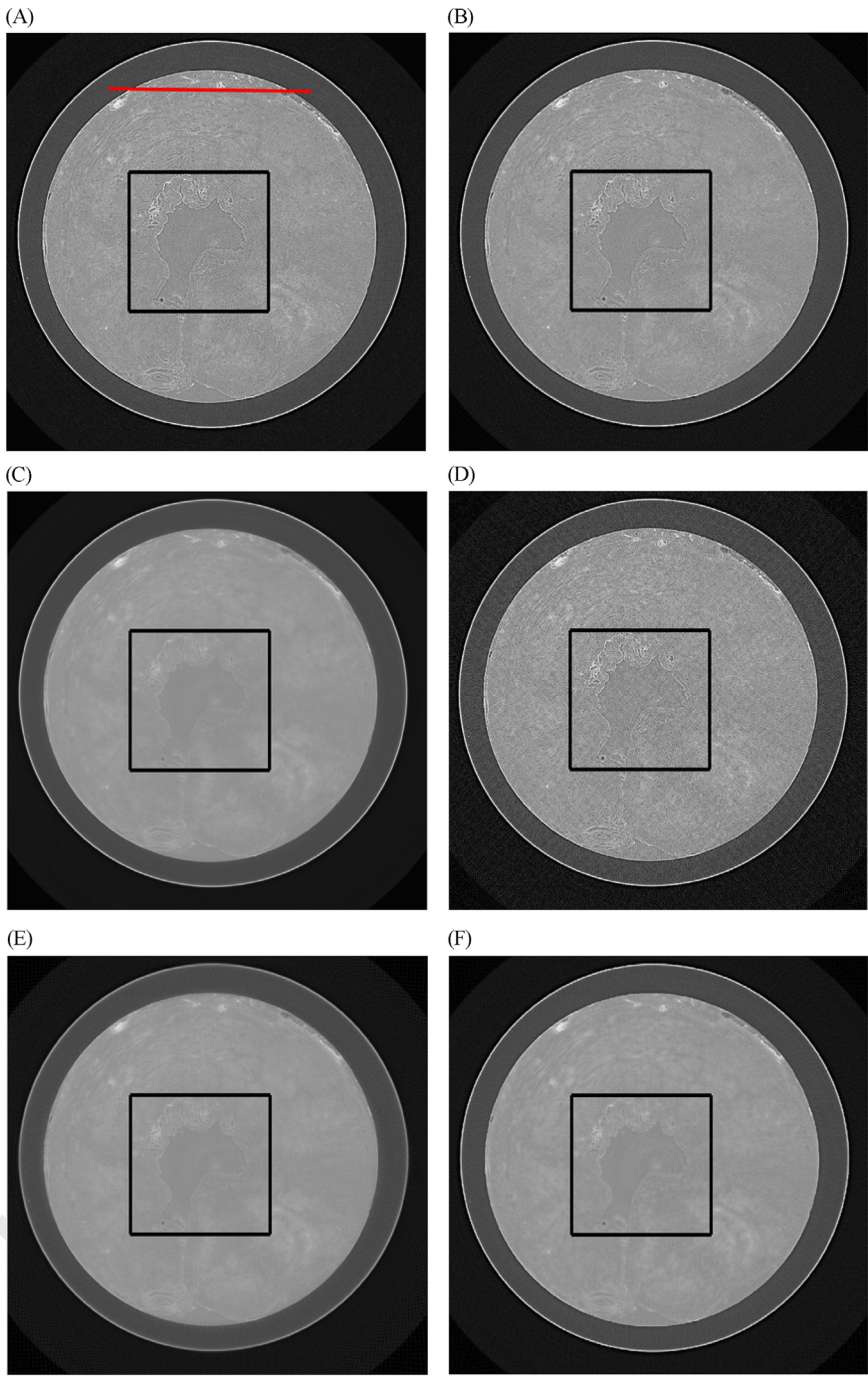


Fig. 5. Reconstructed canine prostate slice with 20% of projected data; the corresponding zoomed areas are shown in Fig. 6 (A) Reference, (B) Proposed, (C) MLEM, (D) FBP, (E) POCS, (F) ASD-POCS.

because the reconstruction is almost perfect for this algorithm. The enlarged image areas are shown in Fig. 3 to better illustrate the quality of the reconstructed images. As shown in Figs. 1–3, FBP reconstructs detailed (high spatial frequency) features such as edges better than POCS and MLEM; however, the POCS and MLEM algorithms can better recover smooth (low spatial frequency) regions and suppress streak artifacts generated by incomplete projected data relative to images reconstructed with FBP. Also, ASD-POCS and the proposed algorithm can recover prominent edges and simultaneously reduce or completely remove streak artifacts which means that these two algorithms are more

successful in forming artifact-resolution trade-off than FBP, POCS and MLEM algorithms.

Table 1 shows the quality metrics for different number of projected data. To better illustrate the effectiveness of the proposed algorithm, the quality metrics are plotted and shown individually in Fig. 4. It can be seen from Table 1 and Fig. 4 that the proposed algorithm has lower reconstruction error and higher structural similarity to the reference image compared with other algorithms. This advantage is the result of combination of the total variation regularizer which is well suited to piecewise smooth images with DRS and randomized Kaczmarz algorithm.

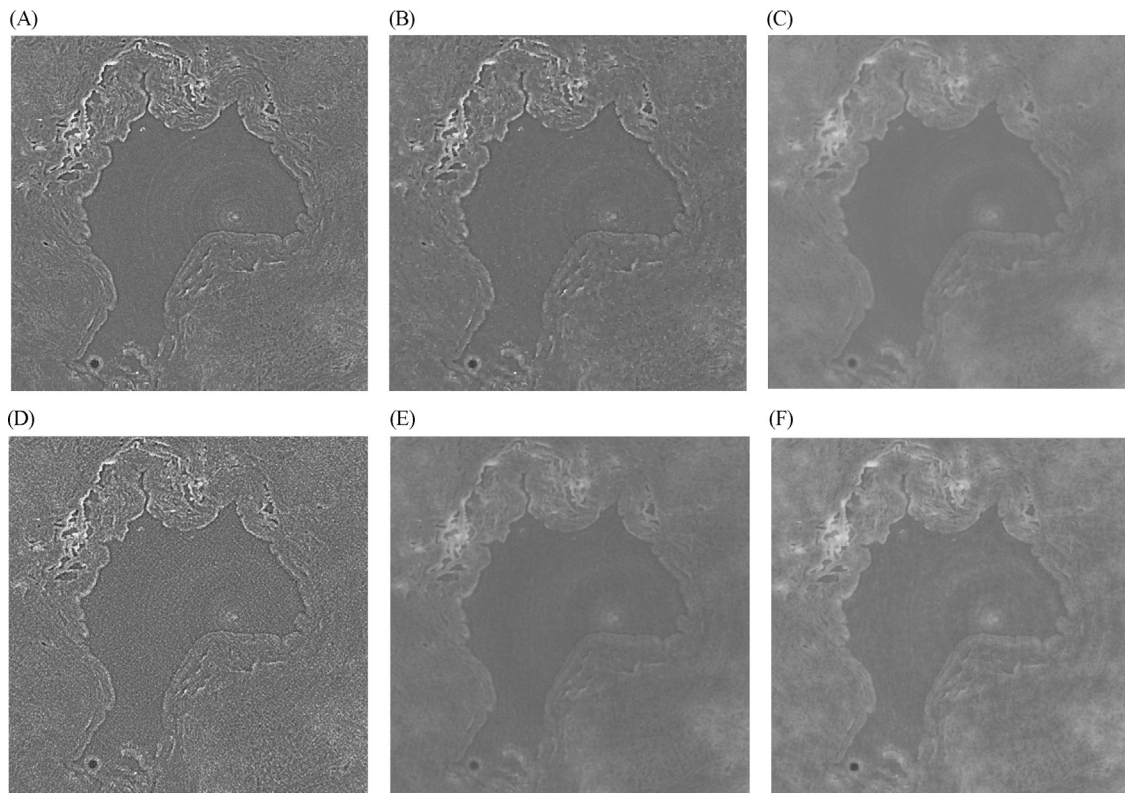


Fig. 6. Zoomed reconstructed canine prostate slice with 20% of projected samples (A) Reference, (B) Proposed, (C) MLEM, (D) FBP, (E) POCS, (F) ASD-POCS.

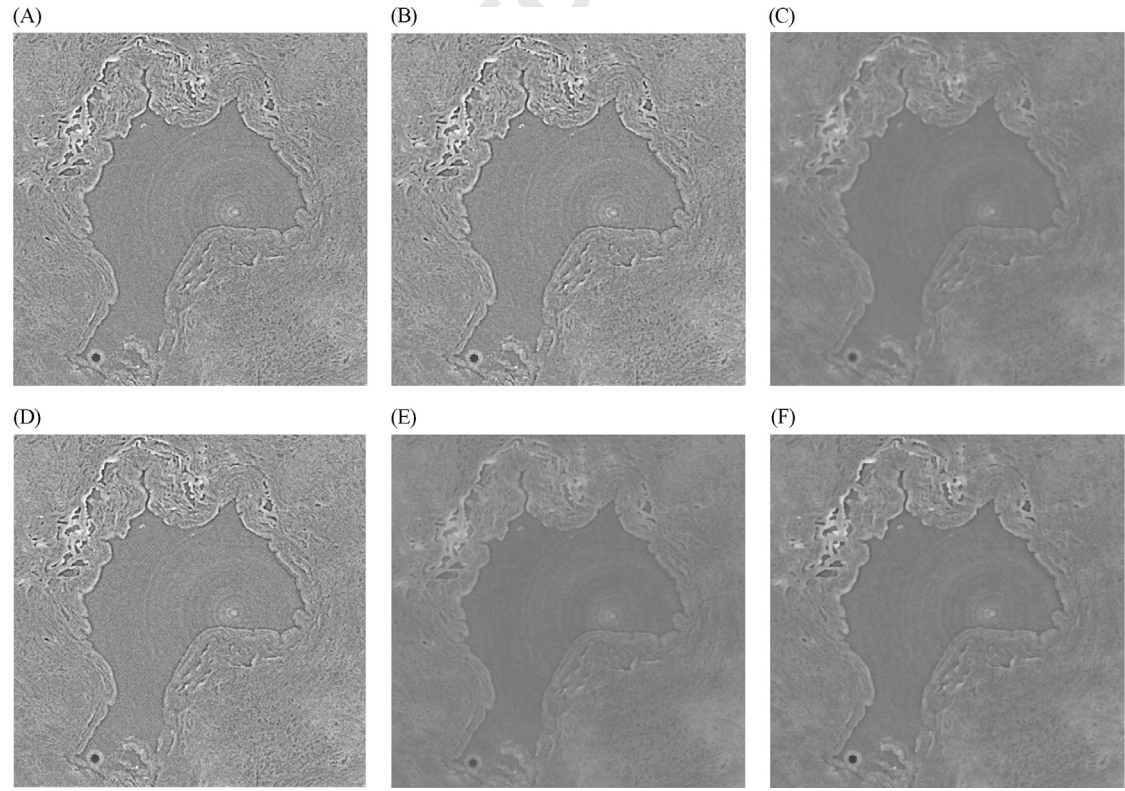


Fig. 7. Zoomed reconstructed canine prostate slice with 50% of projected samples (A) Reference, (B) Proposed, (C) MLEM, (D) FBP, (E) POCS, (F) ASD-POCS.

3.2. Reconstructed images of ex-vivo canine prostate

The proposed algorithm was used to reconstruct a 3.1 mm thick single transverse slice of an ex-vivo canine prostate. The raw data

were collected at the Canadian Light Source by the Prostate Imaging Research Group. A reference image is reconstructed by SkyScan NRecon package using all 3751 projections. The size of the image is 2500 × 2500 pixels. Like before, five images were then reconstructed

Table 2

Quality metrics of reconstructed canine prostate images.

Sample percentage	20% SSIM	RE%	PSNR	30% SSIM	RE%	PSNR	40% SSIM	RE%	PSNR	50% SSIM	RE%	PSNR
Method												
Proposed	0.61	8.55	28.49	0.68	7.33	29.82	0.74	6.43	30.97	0.78	5.72	31.98
FBP	0.38	15.52	23.31	0.53	11.09	26.23	0.54	10.64	26.59	0.70	7.31	29.85
POCS	0.55	13.25	24.68	0.59	12.39	25.27	0.61	11.96	25.57	0.63	11.7	25.76
MLEM	0.54	11.48	25.93	0.56	10.68	26.56	0.58	10.10	27.04	0.62	8.74	28.30
ASD-POCS	0.60	10.49	26.72	0.66	9.09	27.96	0.70	8.27	28.78	0.73	7.73	29.37

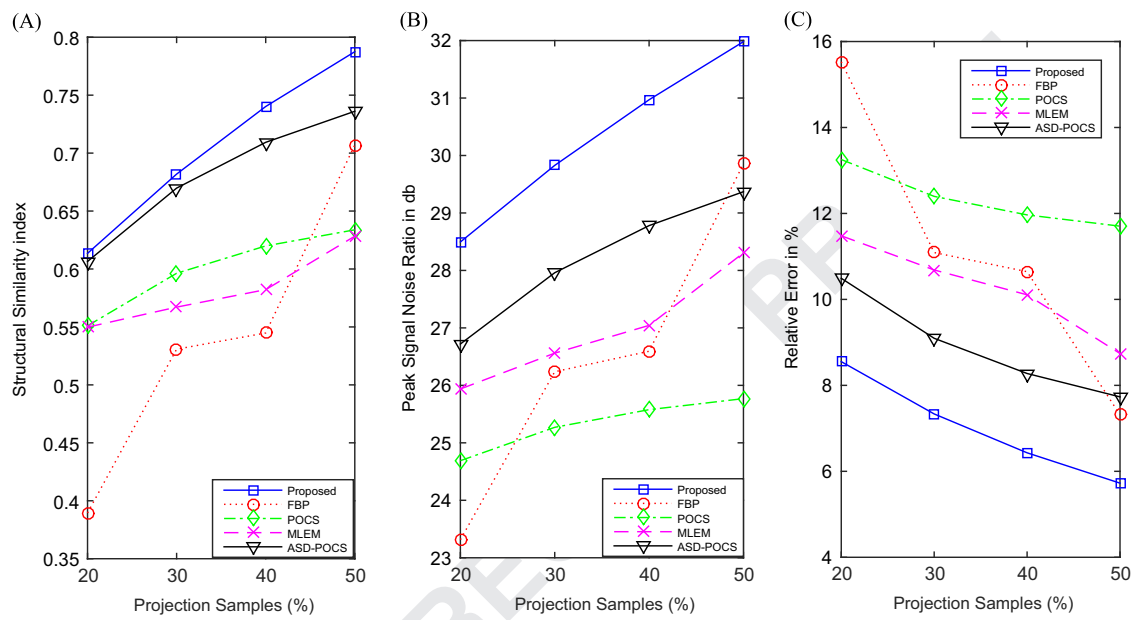


Fig. 8. Canine prostate image quality metrics vs percentage of projected data (A) SSIM, (B) PSNR, (C) RE.

by FBP, POCS, MLEM, ASD-POCS and the proposed algorithm using equally spaced 20%, 30%, 40% and 50% of the full dataset. Figs. 5–7 show the visual comparison among the reference image and reconstructed images using 20% (750 views) and 50% (1875 views) of full dataset. Table 2 shows the three quality metrics, SSIM, PSNR, RE related to different percentages of the projected data. To make clear the advantage of the new proposed algorithm, the quality metrics are plotted separately and shown in Fig. 8. Each quality metric is sensitive to a different aspect of image quality and it is shown that the proposed algorithm is superior in all metrics compared to the existing reconstruction algorithms. Fig. 9 shows the horizontal intensity profile of images reconstructed by the proposed algorithm and other algorithms. These graphs show that the intensity profile of the proposed algorithm was much closer to the reference image intensity profile in non-edge and specifically in edge regions demonstrating its ability to produce superior quality edges.

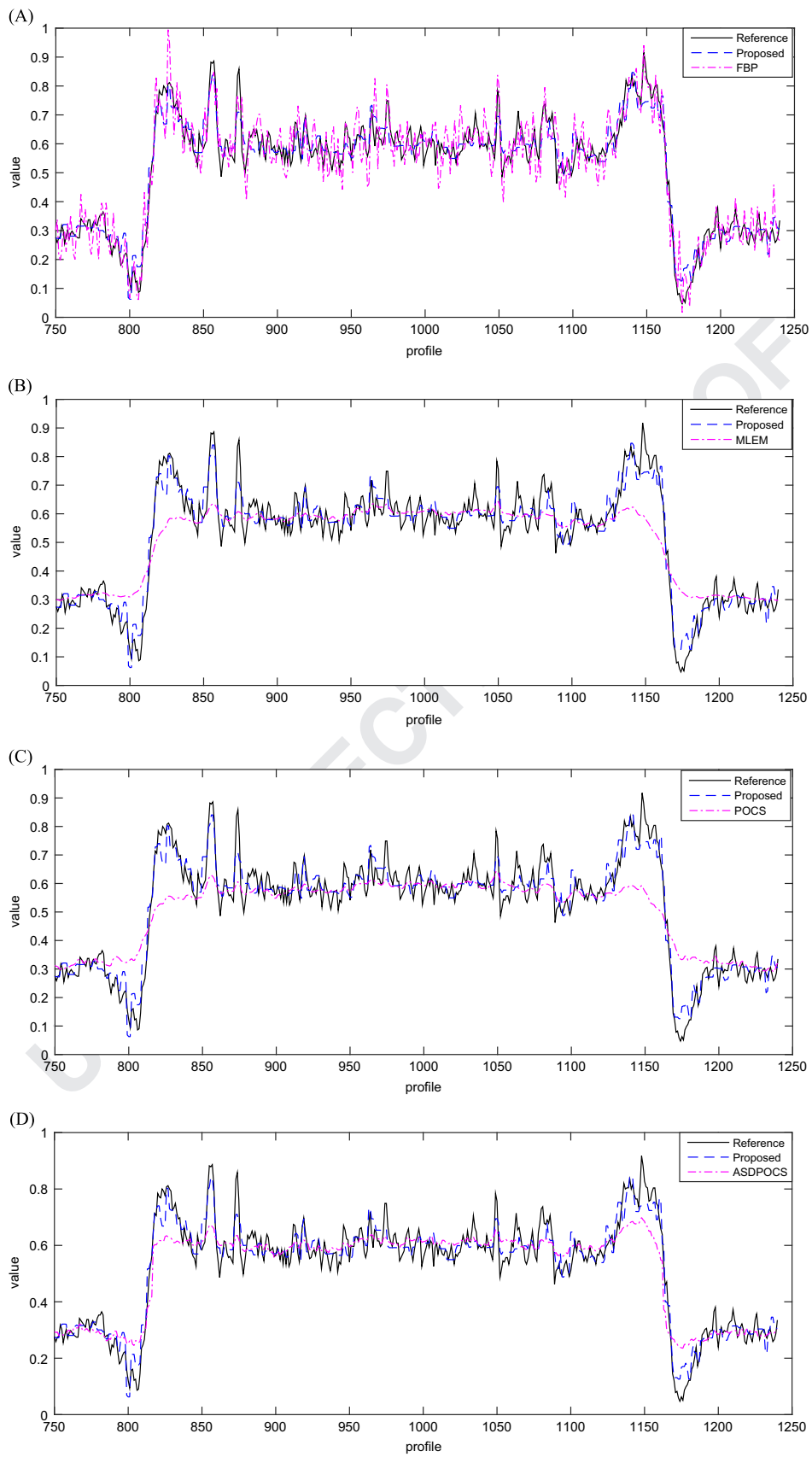
One slice of these reconstructed images is shown in Fig. 5, the prostatic urethra is in the central part of image and is zoomed in Figs. 6 and 7 to better visualize performance of the various algorithms. The FBP reconstructed images in Figs. 6 and 7 and the line profile in Fig. 9 shows a large number of pervasive streak artifacts because of the low sample rate. The resolution and image quality are considerably reduced due to these artifacts. As shown in Figs. 6 and 7 and the line profile in Fig. 9, in the POCS and MLEM images, the streak artifacts and noise are decreased, but residual artifacts are still pervasive especially in the POCS (noise and streak artifacts in the black background surrounding the prostate in Fig. 5). Moreover, blurring artifact is present and low contrast structures are not visible.

It can be seen in Table 2 and Fig. 8 that POCS and MLEM algorithms are better than FBP with respect to existing quality metrics at the lower sampling rate (20%). Contrary to this, FBP is more successful than POCS and MLEM using a higher sampling rate (50%). ASD-POCS applies total variation to remove streak artifacts without generation of undesirable effects but as illustrated in Figs. 6 and 7 a number of low frequency blocky-shaped structures are seen in the smooth regions. In clinical practice, these blocky-shaped structures may obscure the presence of small low contrast details. Finally, as demonstrated in Figs. 6 and 7 and the line profile in Fig. 9, the proposed algorithm is successful in controlling the trade-off between artifact suppression and spatial resolution. We can also see from Fig. 8 that the RE is below 10% and the PSNR is more than 25 dB for the proposed algorithm. These results indicate that high reconstruction accuracy is achieved using the proposed algorithm. As well, from the SSIM value and visual observation of Figs. 6 and 7, one may conclude that the proposed algorithm is capable of suppressing streak artifacts and noise, leading to an image of acceptable quality from a lower number of views.

The future work is directed towards using distributed hardware (such as, cloud computing) with our algorithm to reconstruct images from a very large dataset which is typical in synchrotron based medical tomography.

4. Conclusions

The proposed research reveals the potential of total variation minimization in reconstructing synchrotron source propagation-



Q2 Fig. 9. Intensity profiles (red line in Fig. 5) of reconstructed canine prostate images with 20% of projected data (A) FBP, (B) MLEM, (C) POCS, (D) ASDPOCS. (For interpretation of the references to color in this figure legend, the reader is referred to the web version of this article.)

1 based X-ray phase contrast computed tomography (XPC-CT) by
 2 using a novel combination of Douglas–Rachford Splitting (DRS)
 3 and randomized Kaczmarz algorithms. After applying DRS to
 4 optimize this large-scale non smooth regularized model and using
 5 iterative randomized Kaczmarz algorithm, an optimal balance
 6 between artifact suppression and spatial resolution is obtained.
 7 The algorithm is applied to tomography data collected in the
 8 Biomedical Imaging and Therapy Bending Magnet (BMIT-BM)
 9 beamline at the Canadian Light Source Visual assessment and
 10 quantitative based evaluation metrics are used to show the
 11 superiority of the proposed algorithm with respect to a number of
 12 recognized reconstruction algorithms using different numbers of
 13 projections. The results show that, without compromising image
 14 quality, the radiation dose and imaging time can be reduced which
 15 is an important step towards transitioning to clinically applicable
 16 propagation-based XPC-CT.

Acknowledgments

Q4 Q3 The research is conducted at the Multimedia Processing and Prototyping Lab in the Department of Electrical and Computer Engineering at the University of Saskatchewan which is funded by Natural Sciences and Engineering Research Council of Canada (NSERC), Canada Foundation for Innovation (CFI) and Western Economic Diversification Canada. The authors would like to thank the members of the University of Saskatchewan Prostate Research Team: M. Buhr, J. Singh, G. Belev, R. Chibbar, P. Malhi, K. Visvanathan for helping to collect the canine prostate dataset at the Canadian Light Source. The authors also acknowledge support from the Saskatchewan Health Research Foundation (SHRF), the Saskatoon Chapter of Motorcycle Ride for Dad – Prostate Cancer Fight Foundation, the National Research Council Canada, the Canadian Institutes of Health Research, and the Government of Saskatchewan.

References

- [1] S.W.T.P.J. Heijmink, J.J. Fütterer, S.S. Strum, W.J.G. Oyen, F. Frauscher, J. A. Witjes, J.O. Barentsz, *Acta Oncologica* 50 (Suppl 1) (2011) S25.
- [2] T.J. Davis, D. Gao, T.E. Gureyev, *Nature* 373 (1995) 595.
- [3] S.W. Wilkins, D. Gao, A. Pogany, *Nature* 384 (1996) 335.
- [4] X. Wu, H. Liu, *Journal of X-Ray Science and Technology* 11 (2003) 33.
- [5] T. Tanaka, C. Honda, S. Matsuo, K. Noma, H. Oohara, N. Nitta, *Investigative Radiology* 40 (7) (2005) 385.
- [6] X. Wu, H. Liu, *Medical Physics* 34 (2) (2007) 737.
- [7] A. Bravin, P. Coan, P. Suorrtti, *Physics in Medicine and Biology* 58 (2013) 1.
- [8] L. Tang, G. Li, Y.S. Sun, J. Li, X.P. Zhang, *Journal of Synchrotron Radiation* 19 (2012) 319.
- [9] A. Snigirev, I. Snigireva, V. Kohn, S. Kuznetsov, I. Schelokov, *Review of Scientific Instruments* 66 (12) (1995) 5486.
- [10] P. Cloetens, M. Pateyron-Salomé, J.Y. Buffière, G. Peix, J. Baruchel, F. Peyrin, M. Schlenker, *Journal of Applied Physics* 81 (9) (1997) 5878.
- [11] R. Chen, H. Xie, L. Rigon, G. Du, E. Castelli, T. Xiao, *Tsinghua Science and Technology* 15 (2010) 102.
- [12] B.F. McEwen, K.H. Downing, R.M. Glaeser, *Ultramicroscopy* 60 (1995) 357.
- [13] R.A. Crowther, D.J. DeRosier, A. Klug, *Proceedings of the Royal Society B* 317 (1970) 319.
- [14] A.C. Kak, M. Slaney, *Principles of Computerized Tomographic Imaging*, IEEE Press, New York, 1988.
- [15] T. Wysokinski, D. Chapman, G. Adams, M. Renier, P. Suorrtti, W. Thomlinson, *Nuclear Instruments and Methods in Physics Research A* 582 (1) (2007) 73.
- [16] J. Hsieh, *Computed Tomography Principles, Designs, Artifacts, and Recent Advances*, SPIE Press, Bellingham, WA, 2003.
- [17] J.F. Barrett, N. Keat, *Radiographics* 24 (2004) 1679.
- [18] M. Beister, D. Kolditz, W.A. Kalender, *Physica Medica* 28 (2012) 94.
- [19] G.T. Herman, A. Lent, S.W. Rowland, *Journal of Theoretical Biology* 42-1 (1973) 1.
- [20] L. Shepp, Y. Vardi, *IEEE Transactions on Medical Imaging* 1 (1982) 113.
- [21] E.Y. Sidky, X. Pan, *Physics in Medicine and Biology* 53 (2008) 4777.
- [22] Y. Tsai, D.L. Donoho, *IEEE Transactions on Information Theory* 52 (2006) 1289.
- [23] E.J. Candès, J. Romberg, T. Tao, *IEEE Transactions on Information Theory* 52 (2) (2006) 489.
- [24] L. Ritschl, F. Bergner, C. Fleischmann, M. Kachelriess, *Physics in Medicine and Biology* 56 (2011) 1545.
- [25] J. Douglas, H.H. Rachford, *Transactions of the American Mathematical Society* 82 (1956) 421.
- [26] T. Strohmer, R. Vershynin, *Journal of Fourier Analysis and Applications* 15 (2009) 262.
- [27] E.L. Ritman, *Annual Review of Biomedical Engineering* 6 (2004) 185.
- [28] S. Strengell, J. Keyriläinen, P. Suorrtti, S. Bayat, A.R. Sovijärvi, L. Porra, *Journal of Synchrotron Radiation* 21 (6) (2014) 1305.
- [29] Z.T. Wang, L. Zhang, Z.F. Huang, K.J. Kang, Z.Q. Chen, Q.G. Fang, P.P. Zhu, *Chinese Physics C* 33 (11) (2009) 975.
- [30] B. Wolkowski, E. Snead, M. Wesolowski, J. Singh, M. Pettitt, R. Chibbar, S. Melli, J. Montgomery, *Journal of Synchrotron Radiation* 22 (4) (2015) 1130.
- [31] (<http://bruker-microct.com/next/NReconUserGuide.pdf>).
- [32] R.C. Chen, D. Dreossi, L. Mancini, R. Menk, L. Rigon, T.Q. Xiao, R. Longo, *Journal of Synchrotron Radiation* 19 (5) (2012) 836.
- [33] (<http://imagej.nih.gov/ij/>).
- [34] R. Hegerl, W. Hoppe, *Zeitschrift für Naturforschung* 31a (1976) 1717.
- [35] R. Grimm, H. Singh, R. Rachel, D. Typke, W. Zillig, W. Baumeister, *Biophysical Journal* 74 (1998) 1031.
- [36] C.E. Engeler, *Urology* 40 (4) (1992) 346.
- [37] M. Lustig, D. Donoho, J. Santos, J. Pauly, *IEEE Signal Processing Magazine* 25 (2) (2008) 72.
- [38] A. Bouhamidi, K. Jbilou, *Journal of Computational Mathematics* 206 (2007) 86.
- [39] L.I. Rudin, S. Osher, E. Fatemi, *Physica D* 60 (1992) 259.
- [40] T.F. Chan, S. Esedoglu, F. Park, M.H. Yip, *Recent developments in total variation image restoration*, In: *Handbook of Mathematical Models in Computer Vision*, Springer Verlag, 2005.
- [41] P. Blomgren, T.F. Chan, P. Mulet, C.K. Wong, *Total variation image restoration: numerical methods and extensions*, In: *Proceedings of the International Conference on Image Processing*, 3, 1997, p. 384–387.
- [42] R. Tibshirani, *Journal of the Royal Statistical Society Series B* 58 (1996) 267.
- [43] P. Bertsekas Dimitri, *Constrained Optimization and Lagrange Multiplier Methods*, Athena Scientific, 1996.
- [44] J. Eckstein, D. Bertsekas, *Mathematical Programming* 5 (1992) 293.
- [45] O. Michailovich, *IEEE Transactions on Image Processing* 20 (5) (2011) 1281.
- [46] J. Nocedal, J.W. Stephen, *Least-Squares Problems*, Springer, New York, 2006.
- [47] S. Boyd, N. Parikh, E. Chu, B. Peleato, J. Eckstein, *Foundations and Trends in Machine Learning* 3 (2011) 1.
- [48] P.C. Hansen, M. Saxild-Hansen, *Journal of Computational and Applied Mathematics* 236 (8) (2012) 2167.
- [49] Z. Wang, A.C. Bovik, H.R. Sheikh, E.P. Simoncelli, *IEEE Transactions on Image Processing* 13 (2004) 600.
- [50] (<http://www.imp.uni-erlangen.de/phantoms/>).